Single-protein nanomechanical mass spectrometry in real time

M.S. Hanay[+1], S. Kelber[+1], A.K. Naik[11], D. Chi[1], S. Hentz[2,1], E.C. Bullard[1], E. Colinet[2,1], L. Duraffourg[2], M. L. Roukes[*1]

[1]Kavli Nanoscience Institute and Departments of Physics, Applied Physics, and Bioengineering, California Institute of Technology, MC 149-33, Pasadena, CA, 91125 USA

[2] CEA-Leti, MINATEC Campus, 17 Rue des Martyrs, 38054, Grenoble Cedex 9, France

Equations for the Determination of Mass and Position

We model the adsorption of analytes upon a NEMS resonator as that of point particles accreting instantaneously and rigidly upon the device. Since the added molecule/particle is concentrated as a globular entity with a localized site of binding rather than extended over the beam, its contribution to the elastic energy of the total system is small compared to the effect of mass on the kinetic energy. Our discussion follows the Supplementary Information section of Ref. 1 and uses a slightly different notation with respect to the main text in order to increase the readability of the mathematical expressions in this section. A point particle of mass Δm landing on a NEMS resonator, itself with total mass of M_{total}, will shift the resonator's frequency according to the following:

$$\Delta f_n = -\frac{f_n}{\alpha_n M_{total}} \Delta m \; \phi_n\left(a\right)^2 \tag{1}$$

Here f_n denotes the natural resonant frequency of nth mode of the device, M_{total} represents the (actual) device mass and $\phi_n(a)$ denotes the nth resonance mode shape at the normalized landing position, a, with the normalization condition $\max(\phi_n(a)) = 1$. The term α_n is a numerical factor defined as:

$$\alpha_n = 2 \int_{a=0}^{a=1} \phi_n(a)^2 \, da \tag{2}$$

which characterizes the effective mass for each mode $M_{eff}^{(n)} = (\alpha_n / 2) M_{total}$. The limitations of the aforementioned assumption are minimal for the devices employed in this work. All NEMS resonators employed have appreciable cross section compared to the dimensions of the individual accreting species. In cases where this fails to hold, individual adsorbates can affect the mode shape, and potentially the quality factor of the resonance. In these situations, analysis will involve a more complex formalism than presented here. Further, in these experiments the NEMS device is maintained at

---

[+] These authors contributed equally to this work.
[1] Present address: Centre for Nano Science and Engineering, Indian Institute of Science, Bangalore, Karnataka, India
[*] Corresponding Author: **roukes@caltech.edu**

reduced temperatures where physisorption of the accreting species is sufficient to anchor them. For cases where this fails to hold, richer dynamics ensues[2-5].

Defining the normalized mass change as $\delta m \equiv \Delta m / M_{total}$ and the normalized frequency shift as $\delta f = \Delta f / f_0$, the first equation can be written as:

$$\delta m \, \phi_n (a)^2 = -\alpha_n \, \delta f_n \tag{3}$$

Using the first two modes of the NEMS resonator, the above equation can be written as:

$$\frac{\phi_1 (a)^2}{\phi_2 (a)^2} = \frac{\alpha_1 \, \delta f_1}{\alpha_2 \, \delta f_2} \tag{4}$$

For a doubly-clamped beam, the mass δm and the position a can be determined from the first two modes of the NEMS resonator if the function, defined as:

$$G(a) \equiv \phi_1 (a)^2 / \phi_2 (a)^2 \tag{5}$$

is invertible, *i.e.* if a single valued $G^{-1}[\delta f_1, \delta f_2]$ exists. In this case, we could obtain the position by:

$$a = G^{-1}(\frac{\alpha_1 \, \delta f_1}{\alpha_2 \, \delta f_2}) \tag{6}$$

A smooth function is invertible, if it is *one-to-one* and *onto*. The function $G(a)$ is plotted in Figure 1c (main text) for a doubly-clamped beam. Although this function is onto, it is not a one-to-one function and thus cannot be used to evaluate a single value for the position, a.

However because of the inherent symmetry of the doubly-clamped beam, the two position solutions for equation (3) are equidistant from the center of the beam:

$$\phi_1 (a_1)^2 = \phi_1 (a_2)^2 \tag{7}$$

$$\phi_2 (a_1)^2 = \phi_2 (a_2)^2 \tag{8}$$

These two solutions yield the same mass value:

$$\delta m = \frac{-\alpha_1 \, \delta f_1}{\phi_1 (a_1)^2} = \frac{-\alpha_1 \, \delta f_1}{\left(\phi_1 \left(G^{-1}[\delta f_1, \delta f_2]\right)\right)^2} \tag{9}$$

Note that the above statement is only true for the first two modes of the doubly-clamped beam. An arbitrary choice of two modes of the doubly-clamped beam would not, in general, result in a single valued G even after accounting for the symmetry of the device. In general, it is therefore important to

choose the appropriate modes or expand the analysis. For a cantilever, for example, the mass and position of the species landing on the NEMS resonator can be determined if the first three cantilever modes are used [6].

Modeling of Frequency Noise as Random Variables

Usually, the standard deviation is used to characterize the dispersion of a statistical variable. However for frequency measurements, standard deviation happens to be a rather poor measure for quantifying dispersion, since it depends on the sample size (N) and does not converge for certain types of frequency noise commonly encountered in experiments. Prominent among these are flicker noise and drift (random walk noise) [7]. A better measure that has been devised to characterize the frequency noise is the Allan deviation. To calculate the Allan deviation, we first consider the fractional frequency difference, y[n], for each discrete time index n:

$$y[n] = \frac{f[n] - f_0}{f_0}$$ (10)

Here f_0 is the nominal frequency of the resonator and $f[n]$ is the measured frequency of the NEMS resonator at the time step $[n]$. With this convention, the Allan variance σ_{Allan}^2 is defined as:

$$\sigma_{Allan}^2 \equiv \frac{1}{2(N-1)} \sum_{n=1}^{n=N-1} \left(y[n+1] - y[n] \right)^2$$ (11)

The Allan deviation is the square root of this quantity.

The frequency stability of a resonator depends also on the time scale over which it is observed. For example, one particular resonator might be very stable for short periods of time, but it may drift appreciably when observed over longer time scales. This kind of dependence on timescale can be reflected by the Allan deviation as well. The definition of the Allan deviation shown above is calculated for the fastest time scale, *i.e.* the sampling bandwidth, of the measurement. To calculate the Allan deviation over longer timescales, the data is sliced into time segments, each having the size of the relevant physical timescale (Figure S1a). The average of each segment is then determined, and the Allan deviation for an ensemble composed of these averaged values is calculated. For instance, if the timescale of interest is τ, such that $\tau = q\, T_{Sampling}$ with q being some integer, then:

$$\sigma_{Allan}^2(\tau) = \frac{1}{2(M-1)} \sum_{m=1}^{M} \left(\overline{y[m+1]} - \overline{y[m]} \right)^2$$ (12)
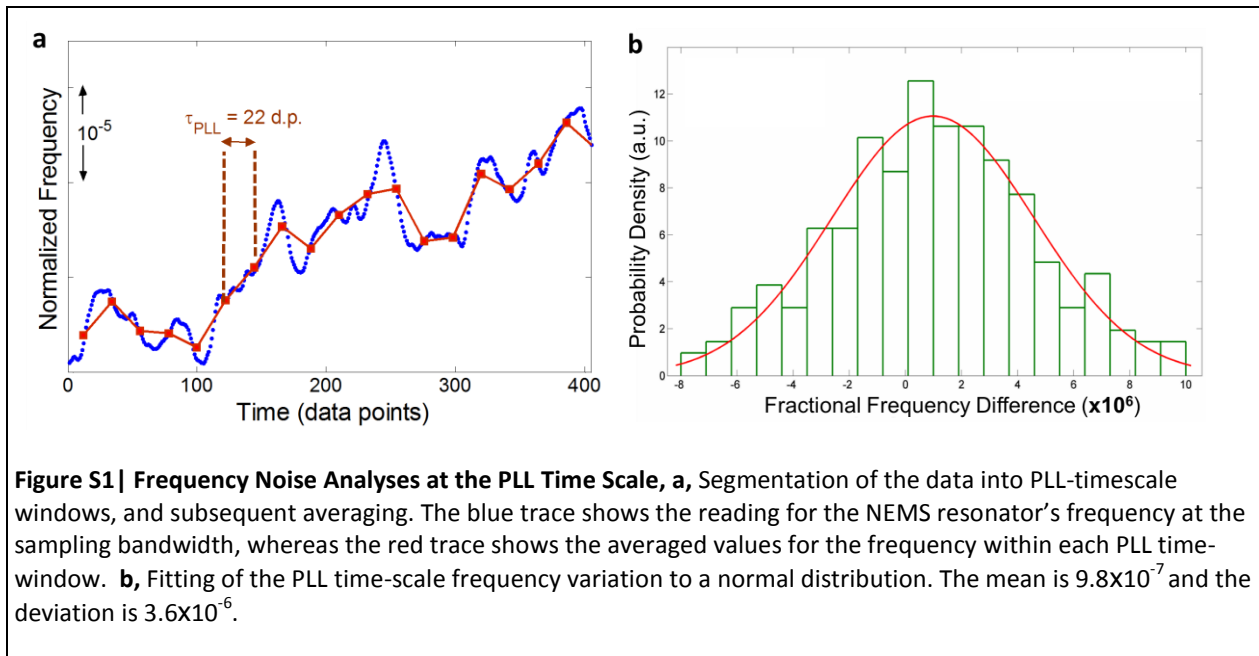
Here $\overline{y[m]}$ shows the average value of the fractional frequency difference, during the time interval denoted by m. Also $M = N/q$, since we slice a total of N data points into segments containing q data points.

While the Allan deviation is a scalar parameter that characterizes the frequency noise, it does not contain a representation of all characteristics about the random fluctuations. We can provide additional information about these fluctuations if we define a probability density function (**PDF)** for the frequency noise. Here our first goal is to estimate the PDF of the frequency noise from the experimental data. After measuring the fractional frequency difference, $y[n]$, we can fit the resulting ensemble within a typical PDF model. As a first approach, we employ a Gaussian distribution, which seems to model the frequency noise in our experiments sufficiently well. The variance in the Gaussian distribution has a value similar to the Allan variance– as both parameters quantify the dispersion of the NEMS frequency.

A typical time trace from an actual measurement is shown in Figure S1a, along with the smoothing operation carried out at the PLL time scale, which is 8.8 seconds or 22 data points in this case, as determined by independent measurements. The histogram for fractional frequency difference at the PLL timescale is shown in Figure S1b. The distribution of the frequency noise for this timescale appears to be a normal distribution , and the PDF is:

$$PDF_{\delta f}\left(\delta f = x\right) = \frac{1}{\sqrt{2\pi}\sigma} e^{\frac{-\left(x-\mu\right)^2}{2\sigma^2}} \tag{13}$$

$with\ \mu = 9.8 \times 10^{-7}\ and\ \sigma = 3.6 \times 10^{-6}$

Figure S1| Frequency Noise Analyses at the PLL Time Scale, a, Segmentation of the data into PLL-timescale windows, and subsequent averaging. The blue trace shows the reading for the NEMS resonator's frequency at the sampling bandwidth, whereas the red trace shows the averaged values for the frequency within each PLL time-window. **b,** Fitting of the PLL time-scale frequency variation to a normal distribution. The mean is 9.8×10^{-7} and the deviation is 3.6×10^{-6}.

Frequency Jumps as Statistical Variables

When a particle lands on the beam, an abrupt frequency shift is measured. This *measured frequency shift* contains some amount of *frequency noise* that degrades the measurement. In the ideal case of no noise, the frequency shift due to the landing event would be:

$$\Delta f_{ideal} \equiv -\alpha \phi(a)^2 \delta m \tag{14}$$

In the presence of noise, the measured value is different:

$$\Delta f_{measured} = \Delta f_{ideal} + \tilde{f}_{noise} \tag{15}$$

The term $\tilde{f}_{noise}$ denotes the frequency noise term in the measurement of which only a statistical description is available. The best estimate for *the ideal frequency shift* ($\Delta f_{estimate}$) is:

$$\Delta f_{estimated} = \Delta f_{measured} - \tilde{f}_{noise} \tag{16}$$

This estimate for the frequency jump can be treated as a random variable. Using the inverse probability theorem, this random variable is centered at the measured frequency jump and has the same statistical distribution as the frequency noise[8]:

$$PDF_{jump}\left(\Delta f\right) = PDF_{noise}(\Delta f - \Delta f_{measured}) \tag{17}$$

Here $PDF_{jump}(\Delta f)$ denotes the probability distribution of the new statistical variable, *the frequency jump,* calculated for frequency change, Δf. On the right hand side, $PDF_{noise}(\Delta f - \Delta f_{measured})$ denotes the probability distribution of the *frequency noise* calculated for the frequency change of $\Delta f - \Delta f_{measured}$. The equation above simply states that when we measure a frequency shift, we can represent it statistically by translating the frequency noise PDF by the amount of the frequency shift. Notice that if the signal-to-noise ratio of the measurement is good, then this new random variable is sharply concentrated around the measured frequency shift. The main reason for such a simple transformation within the Bayesian formalism is that we do not have any prior information about the statistical nature of the frequency jumps beforehand.

Representation of Two-Mode Frequency Jumps

To account for the two statistical variables and their correlations, joint-probability density function formalism can be used. For the two mode data obtained in our experiments, a bivariate Gaussian distribution works satisfactorily. A joint Gaussian distribution for the frequency noise of the two modes is described mathematically in the following form:
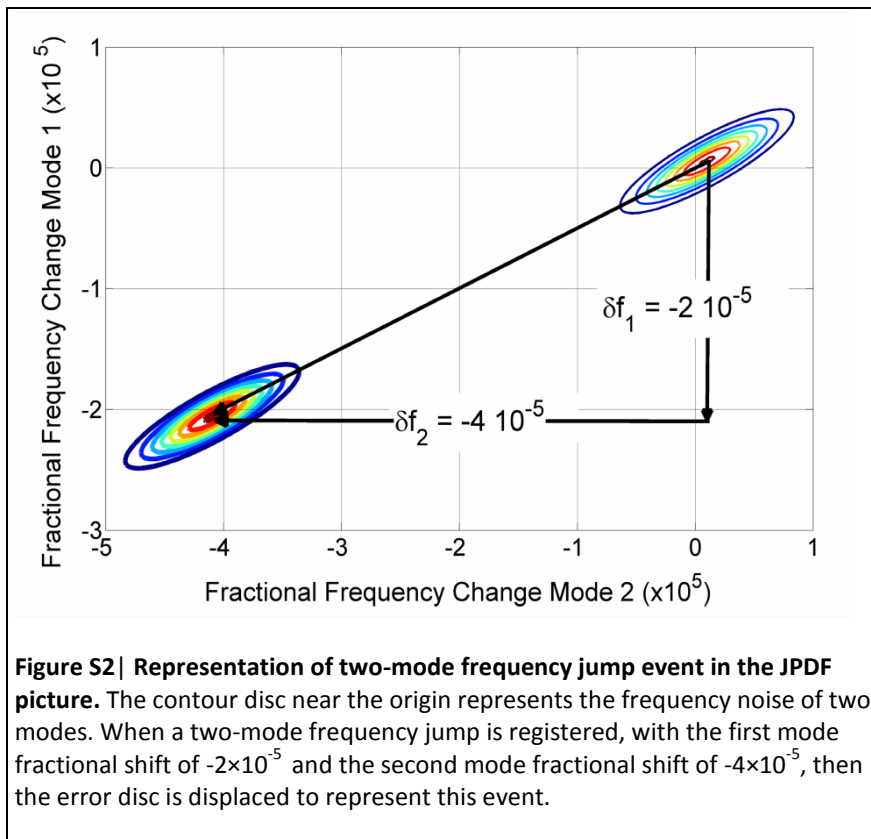
$$JPDF_{\delta f_1, \delta f_2}\left(\delta f_1, \delta f_2\right) = \frac{1}{2\pi\sigma_1\sigma_2\sqrt{\left(1-\rho^2\right)}} exp\left(-\frac{z}{2\left(1-\rho^2\right)}\right) \tag{18}$$

where:

$$z \equiv \frac{\left(\delta f_1 - \mu_1\right)^2}{\sigma_1^2} - \frac{2\rho\left(\delta f_1 - \mu_1\right)(\delta f_2 - \mu_2)}{\sigma_1 \sigma_2} + \frac{\left(\delta f_2 - \mu_1\right)^2}{\sigma_2^2} \tag{19}$$

Here δf_1 and δf_2 represent the normalized frequency shifts in the first and second modes respectively. μ_1 and μ_2 are the mean values for frequency fluctuations, which can be negligible if the frequency of the resonator does not drift strongly. The symbols σ_1 and σ_2 represents the standard deviations of the two modes. The symbol ρ shows the correlation coefficient between the frequency noise in the two modes.

Once we have modeled the two-mode frequency noise with the JPDF formalism above, we can represent the frequency jumps using this JPDF as done above for the single mode case. A frequency jump due to a particle landing can be represented by a displacement of the noise JPDF by the vector formed by the two frequency shifts, as shown in Figure S2. Once we measure frequency shifts $\delta f_1{}'$ and $\delta f_2{}'$ then the JPDF describing this event has the same form as equation (19) with the appropriate substitutions.

Figure S2| Representation of two-mode frequency jump event in the JPDF picture. The contour disc near the origin represents the frequency noise of two modes. When a two-mode frequency jump is registered, with the first mode fractional shift of -2×10^{-5} and the second mode fractional shift of -4×10^{-5}, then the error disc is displaced to represent this event.

Transformation of Uncertainties from Frequency Shifts Domain to Mass-Position Domain

For a given frequency jump, we can obtain $JPDF_{\delta f_1, \delta f_2}(\delta f_1, \delta f_2)$. These two variables, δf_1 and δf_2, can be mapped onto two variables, mass and position – δm and a. To calculate the joint-PDF for mass and position, $JPDF_{\delta m, a}(\delta m, a)$, we can use the bivariate PDF transformation [9] given by:

$$\text{JPDF}_{\delta\text{m, a}}\left(\delta\text{m, a}\right) = |J| \times \text{JPDF}_{\delta f_1, \delta f_2}\left(h_1\left(\delta m, a\right), h_2\left(\delta m, a\right)\right) \tag{20}$$

Here $h_1(\delta m, a)$ and $h_2(\delta m, a)$ are the functional forms for δf_1 and δf_2, respectively (e.g. $\delta f_1 = h_1(\delta m, a)$). Thus, from equation (3) we have: $h_1(\delta m, a) = -\delta m\, \phi_1(a)^2 / \alpha_1$ and $h_2(\delta m, a) = -\delta m\, \phi_2(a)^2 / \alpha_2$. **J** denotes the Jacobian matrix, and **|J|** is the positive determinant of the matrix:

$$|J| = abs\left(\frac{\partial h_1}{\partial(\delta m)}\frac{\partial h_2}{\partial a} - \frac{\partial h_2}{\partial(\delta m)}\frac{\partial h_1}{\partial a}\right) \tag{21}$$

Using this formalism and previous results for the PDF of the frequency shifts, we can calculate the joint-PDF for the mass and position:

$$JPDF_{\delta m, a}\left(\delta m, a\right) = |J| \times \frac{1}{2\pi\sigma_1\sigma_2\sqrt{1-\rho^2}}\exp\left(-\frac{\Gamma}{2\left(1-\rho^2\right)}\right) \tag{22}$$

with the positive determinant of the Jacobian explicitly written as:

$$|J| = \frac{2\delta m}{\alpha_1\alpha_2}\left[\phi_1\left(a\right)\phi_2\left(a\right)\right]\left|\frac{\partial\phi_1}{\partial\eta}\right|_{\eta=a}\phi_2\left(a\right) - \frac{\partial\phi_2}{\partial\eta}\bigg|_{\eta=a}\phi_1\left(a\right)\right| \tag{23}$$

and the term in the exponential given as:

$$\Gamma = \frac{\left(\dfrac{\delta m\, \phi_1\left(a\right)^2}{\alpha_1}+\mu_1\right)^2}{\sigma_1^2} - \frac{2\rho\left(\dfrac{\delta m\, \phi_1\left(a\right)^2}{\alpha_1}+\mu_1\right)\left(\dfrac{\delta m\, \phi_2\left(a\right)^2}{\alpha_2}+\mu_2\right)}{\sigma_1\sigma_2} + \frac{\left(\dfrac{\delta m\, \phi_2\left(a\right)^2}{\alpha_2}+\mu_2\right)^2}{\sigma_2^2} \tag{24}$$

As in the single-mode case, μ_1 and μ_2 are the numerical values for the frequency shifts measured in the first and second modes respectively.
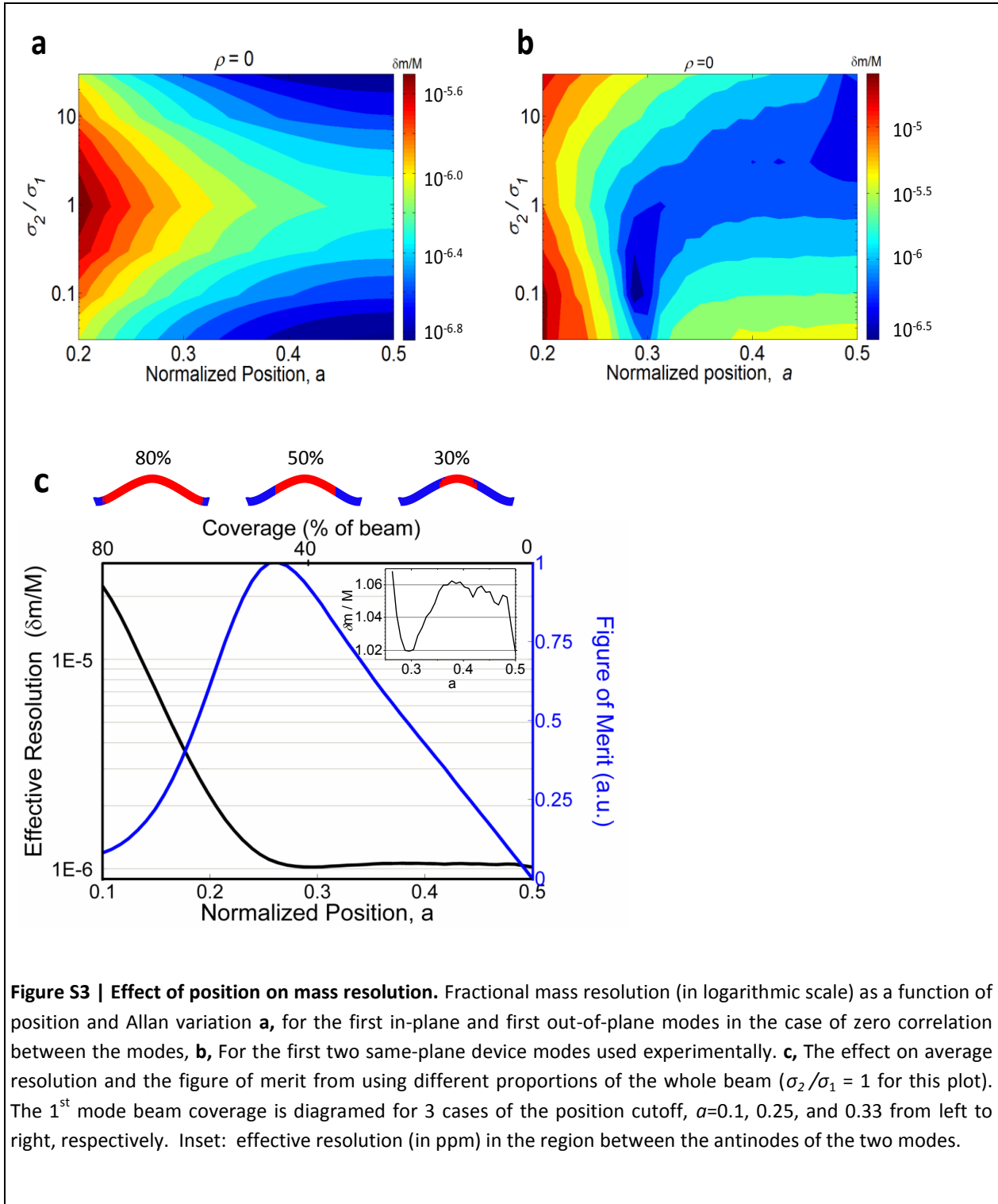
Noise Transformations

These noise-transformation relations can be used to systematically analyze the effect of various parameters on the performance of mass spectrometry experiments. We note the following important points:

i) Mass Resolution.   When two modes have similar noise performance, optimal mass resolution is achieved only for molecules landing on the points of maximum deflection for either mode. For other positions, the resolution is degraded. In NEMS based mass spectrometry measurements, molecules arrive randomly along the length of the NEMS. The mass spectra are then assembled piece-wise at the single molecule level. The mass measurement for events at either end of the device would contribute to a larger error in the mass and effectively degrade the mass resolution. This corrupting influence on mass resolution can be reduced by sacrificing the effective capture cross-section of the NEMS and using only the mass data obtained from the sensitive part of the NEMS. Figure S3c shows the effective mass resolution of the NEMS for different capture cross-sections. The mass resolution is almost constant for the center 50% of the beam ($0.25 \leq a \leq 0.50$) and degrades quickly beyond this region. The figure of merit, defined as the capture cross-section divided by mass resolution, is plotted in Fig. S3c for different values of capture cross-section. This figure suggests that the optimal operational region of the NEMS beam is the center 50% and this conclusion can be used in experimental analysis to pick the frequency shift events such that $a \geq 0.25$. Higher beam modes can be used to extend the useful area of the beam.

ii) Frequency Stability.   Often the noise in the higher modes is larger than that observed in the lower modes and it is important to determine how the mass resolution is affected as higher frequency modes are involved in the experiment. As the relative noise level between the two modes is varied, the mass resolution changes, a behavior depicted in Fig. S3a for the instructive case of two modes with identical mode shapes. The two modes in this case are the fundamental in-plane and out-of-plane modes and the mass resolution is symmetrical with respect to the interchange of these modes due to their geometric equivalence. On the other hand, when two modes have different mode shapes, the geometric difference manifests itself in the mass resolution plot, as sweet spots emerge near the anti-nodes of these modes as shown in Fig. S3b, a plot for the first two modes used in our experiments. In this plot, when two modes have similar Allan variances, the mass resolution is almost constant in the center 40% of the beam. As one of the modes becomes noisier, the region of the beam closer to the anti-node of the noisy mode becomes less responsive as expected. This can have a significant effect on the capture cross-section as well as the effective mass resolution in mass spectrometry measurements.

iii) Correlation of Noise. Figure S4 shows the effect of the noise correlation between the first two modes on the position and the mass measurements. For uncorrelated noise statistics it is evident that the mass resolution stays fairly constant for the center 50% of the beam. As the correlation increases, the degrading effects are predominantly observed at positions where the mode displacement of both the modes is significant. A correlated noise in the two modes can thus affect the effective mass resolution adversely and is therefore undesirable.

Figure S3 | Effect of position on mass resolution. Fractional mass resolution (in logarithmic scale) as a function of position and Allan variation **a,** for the first in-plane and first out-of-plane modes in the case of zero correlation between the modes, **b,** For the first two same-plane device modes used experimentally. **c,** The effect on average resolution and the figure of merit from using different proportions of the whole beam ($\sigma_2/\sigma_1 = 1$ for this plot). The 1st mode beam coverage is diagramed for 3 cases of the position cutoff, a=0.1, 0.25, and 0.33 from left to right, respectively. Inset: effective resolution (in ppm) in the region between the antinodes of the two modes.

Experimental Setup and Device Fabrication for the ESI NEMS-MS System

The NEMS-MS experiments employing electrospray ionization (ESI) were carried out on a table-top vacuum system equipped with a flow cryostat. The flow cryostat is used to cool down a sample stage within a high vacuum chamber on which the NEMS resonator was mounted. The setup consists of three differentially-pumped chambers, an electrospray ionization system (ESI) and a hexapole ion guide (Figure S5a). The ESI process is a well-established technique to create charged particles from solutions [10,11] and the ESI subsystem of the setup is similar to our previous work [1].

Data Collection: The ESI experiments with gold nanoparticles are carried out by injecting solution into a needle (0.3 mm in radius) that is biased at 4 kV. This large voltage causes the emission of charged microdroplets, which subsequently undergo cycles of evaporation and Coulombic fission, until individual ionized particles emerge in the gas phase. These ions are transported into the first stage of vacuum system by hydrodynamic flow and electrostatic focusing. Near the entrance of the vacuum system, hot N_2 gas flows counter to the incoming material. This gas sweeps away neutral molecules and dries out the micro-droplets, enhancing Coulombic fission. Once they have entered into the vauum system, the particles travel through a long capillary toward the first stage of

Figure S4| Effect of Correlation on Noise. Mass resolution (in logarithmic scale) as a function of position for different values of correlation coefficients and Allan variations. When the two modes have significantly different noise values, the sensitivity suffers where the more noisy mode has an antinode (*a=0.5* for mode 1, and *a=0.29* . These maps are obtained with the constraint $\sigma_1\sigma_2 = const$. in order to emphasize the geometric effect of the both modes .

the vacuum chamber. At the end of the tube, the incoming gas expands into a low vacuum region where it is supersonically accelerated. The ions are then sampled by a skimmer structure to obtain a collimated molecular/ionic beam. The larger particles in this molecular beam are slowed down in the second chamber (at 10 mTorr) through collisions with the background atoms. This decelerated beam is focused to the third chamber (main chamber) where the NEMS device is placed.

For the ESI experiments with IgM, several parameters were changed to facilitate the analysis of the protein complex. The ESI needle for IgM experiments had a tip diameter of 20 μm (Picotip Emitter, New Objective), placed about 1 cm away from the vacuum system inlet. The N_2 gas was not heated for IgM experiments. The capillary-skimmer voltage difference was decreased to 30V in order to avoid excessive acceleration of the ions. However, we suspect that the acceleration of the ions due to the supersonic jet flow between the capillary and skimmer regions is already enough to cause a certain degree of fragmentation in the subsequent chambers. The pressure in the collisional focusing cell was elevated to 50 MTorr to facilitate the deceleration of the ions. In both cases, the hexapolar ion guides were driven by alternating RF signals with 350-500 kHz frequencies and 300-360V amplitudes.

Device Fabrication: NEMS device fabrication follows our previous work [12]. For the fabrication of NEMS resonators used in the GNP measurements with the ESI setup, we used 100 nm low-stress silicon nitride on silicon wafers. We fabricated the gold electrodes symmetrically at the two edges defining the NEMS resonators using e-beam lithography and thermal evaporation. Later, we deposited SrF_2 as an etch mask, again using e-beam lithography and thermal evaporation. We suspended the devices using anisotropic and isotropic plasma etching. We removed the etch mask by dipping the chip into HCl. Figure S5b shows the SEM image of one of the devices used in the experiment. The gold electrodes patterned on the beam are used to actuate and measure the mechanical motion via thermoelastic actuation [12] and piezoresistive detection [13], respectively. The resonance curves for the first and two modes are shown in Figure S5(c) and (d). For the IgM experiments with the ESI setup, we have used the devices reported below in the MALDI section.

Experimental Setup and Device Fabrication (MALDI System)

NEMS-MS experiments involving sample introduction by matrix assisted laser desorption ionization (MALDI) were carried out within a table-top, UHV capable apparatus, in a chamber (Kurt Lesker), equipped with a flow cryostat (Janis), used to cool down with liquid Nitrogen to 80K a sample stage on which the NEMS resonator was mounted. The NEMS resonator is placed near the chamber center. The MALDI sample plate is positioned approximately 5mm away from the NEMS resonator on a computer controlled x,y-translation stage (Kurt Lesker). The GNP solution was deposited on the MALDI plate using the drip-dry method; fifteen 2.5ul droplets are applied and then allowed to air dry (Figure S6 (a)).

In general, the MALDI process relies on a compound, termed the matrix, which is used to efficiently absorb laser light and become ionized. The matrix is mixed with the analyte so that when the matrix absorbs the laser light and is ionized, it in turn induces ionization in the analyte, bursting into a plume promoting both species into the gas phase [14]. In our study, we examined gold nanoparticles, which, by themselves, act as matrix [15].

The 5nm GNP solution was concentrated using a centrifuge and washed with water to a particle concentration of 5×10^{14} particles/ml. To one solution glycerol was added at 10% concentration in H_2O. The 10nm solution was similarly washed and concentrated to 1×10^{14} in H_2O and 10% glycerol.

In all cases, the solution was deposited as 2.5ul drops onto the sample plate, with fifteen drops per application (per spot). We allowed the solution to dry between depositions. This last step was done to maximize particle surface density to obtain maximal flux from the MALDI process.
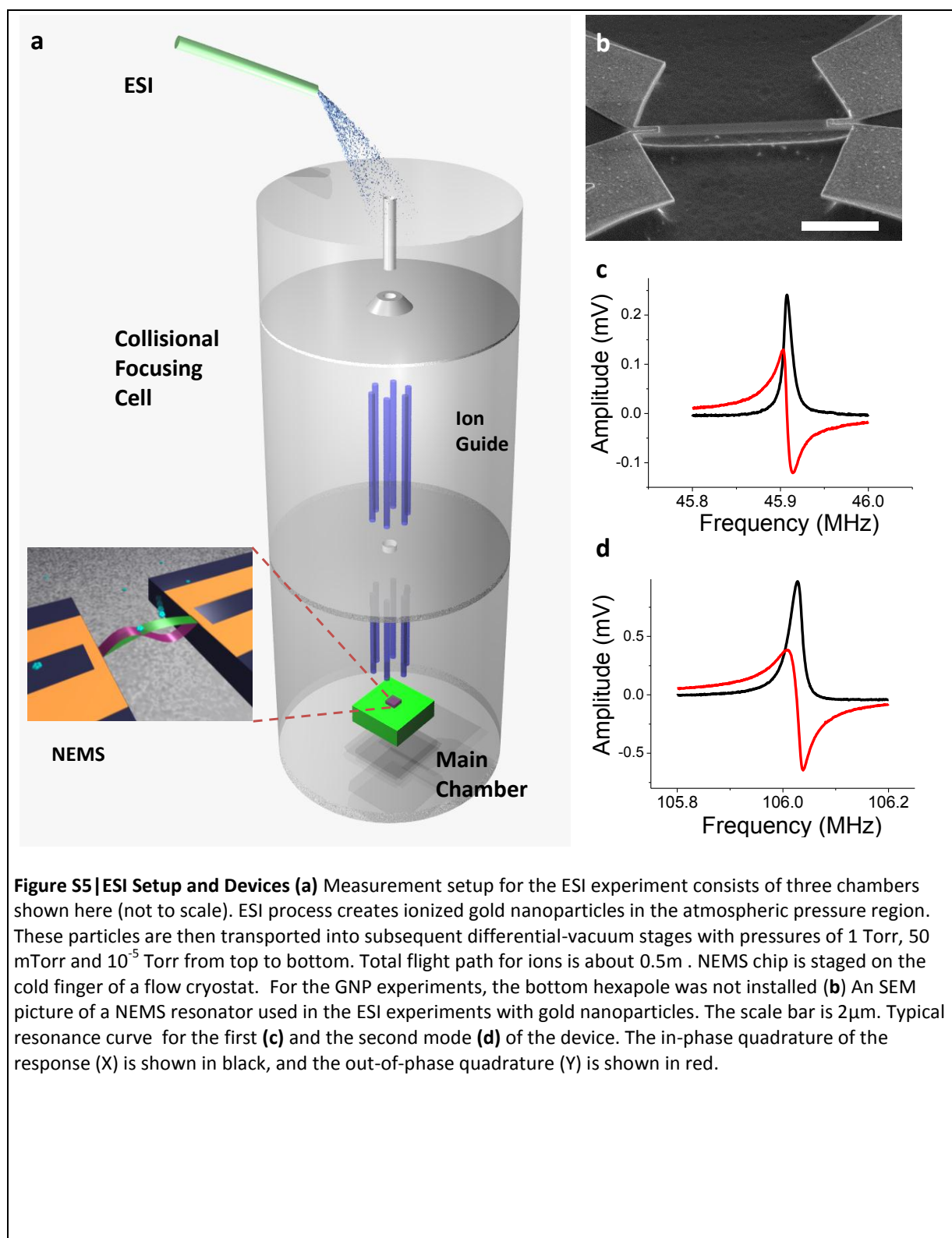
Data Collection: The chamber was pumped down to $\sim1\times10^{-9}$ Torr, and the NEMS device was cooled to $\sim$80K. The MALDI plate was irradiated with laser pulses (337nm, 176µJ/pulse, 3.5ns pulse width, Stanford Research Systems model NL100) at a pulse rate of 1Hz. A 400mm lens (Thorlabs) focused the laser light. A diagram of the setup is given in Figure S6a. The spot on the sample was measured to be $\sim$50x100 um^2 by irradiation tracks left upon a separate thermally-evaporated gold sample. The MALDI sample plate was moved relative to the laser spot using the x-y stage. Particles emitted in the MALDI plume then accreted upon the NEMS resonator. No ionization optics were used, the NEMS resonator collected both positive and negative ions, as well as neutrals, from the MALDI plume.

Device Fabrication: The device employed for these MALDI experiments was fabricated at CEA-LETI/Minatec in Grenoble, France, using similar procedures as described in [16]. Recent work on large-scale integration of NEMS has been described in [17].

Device Calibration

Most of the frequency measurements in this work (IgM measurements with the ESI setup and GNP measurements with the MALDI setup) have been converted into mass values without any calibration, *i.e.* the mass responsivity of the device is exactly what is expected theoretically from equation 1 in the main text. All these measurements use the same type of device and are fabricated by a CMOS compatible top-down process[18].

The only exception to this has been the 10-nm GNP measurements performed with the ESI system using the thermoelastically driven devices as shown in Fig. S5b. Here other independent mass accretion measurements suggest that the responsivity of these devices is about twice of what is theoretically expected. We report the 10-nm ESI GNP data with this calibration – without this calibration we would have obtained 7.8 nm rather than 9.8 nm for these GNP. One possible explanation for this discrepancy between the observed vs. expected responsivity is that the high-density gold electrodes near the edges of the beam contribute to the effective mass of the device because the undercut at the clamps allow the edges to oscillate at larger amplitudes than what is expected using the perfect clamping conditions.

Figure S5|ESI Setup and Devices (a) Measurement setup for the ESI experiment consists of three chambers shown here (not to scale). ESI process creates ionized gold nanoparticles in the atmospheric pressure region. These particles are then transported into subsequent differential-vacuum stages with pressures of 1 Torr, 50 mTorr and 10^{-5} Torr from top to bottom. Total flight path for ions is about 0.5m . NEMS chip is staged on the cold finger of a flow cryostat. For the GNP experiments, the bottom hexapole was not installed (**b**) An SEM picture of a NEMS resonator used in the ESI experiments with gold nanoparticles. The scale bar is 2µm. Typical resonance curve for the first **(c)** and the second mode **(d)** of the device. The in-phase quadrature of the response (X) is shown in black, and the out-of-phase quadrature (Y) is shown in red.

Comparison of ESI and MALDI Techniques

The basis of ESI consists of converting the analytes in a solvent into ionized species in the gas phase. This is accomplished by introducing the solution into a narrow needle kept at high voltage so as to induce Taylor instability at the tip of the liquid and form a spray with charged droplets. These charged droplets then experience cycles of rapid evaporation and Coulombic fission until all the solvent is evaporated and ionized analyte species are formed in the gas phase. In contrast, MALDI introduces samples in the solid phase with an external energy source (a laser) that – through absorption by a matrix chemical premixed with the analyte – both promotes the analytes to vapor phase and ionizes them. The largest difference in these two techniques is the ionization state of the analytes. ESI typically forms analyte ions with much larger charge states than in MALDI[19]. For the purposes of NEMS-MS, this difference in charge states is immaterial. The two most important differences regarding NEMS-based MS are: First, in ESI, transport of analytes to the NEMS sensor requires guiding by ion optics. In MALDI, the desorbed analytes have sufficient kinetic energy to reach the nearby sensor without any ion optics. This allows for smaller, simpler experimental systems. Second, NEMS devices suffer larger environmental noise in ESI Systems. With an ESI injection system, by necessity, there are multiple stages of differential pumping to separate the NEMS device from the analyte solution, which is at atmospheric pressure. Despite these precautions, this still generally leads to higher pressures in the device region that contribute to frequency drift and noise in the NEMS device. This is contrasted with a MALDI-based system where the solid phase analytes are introduced in a vacuum chamber that, after introduction, requires no access to ambient conditions and thus allows for lower pressure in the device region. Finally, MALDI techniques require extensive sample preparation beforehand, especially to avoid bunching of analytes when they are desorbed by the laser. In comparison, ESI pulls apart analytes leading to, in general, less tendency for bunching or clumping of large species. In traditional mass spectrometry a spectra of the same material with the two different ionization schemes would in general be different due to the different charge states of the molecules produced. However, NEMS based mass spectrometry is sensitive to only the inertial mass of the molecule and thus produce nominally the same mass spectra irrespective of the ionization scheme used as shown in Figure 4a.

(Common) Experimental Setup for NEMS-MS Data Acquisition

The NEMS resonators used in this work were controlled and monitored using multimode readout circuitry schematically depicted in Fig. S6b. A piezoresistive down-conversion method was employed for the transduction of the mechanical motion for both cases [20]. For the ESI work with gold nanoparticles, the circuitry follows our recent work closely[12], with additional components (power combiners and filters) to transduce two modes simultaneously. For each mode, one function generator (Rhode and Schwartz model SM03) is used to excite the drive electrode at half the resonance frequency and another function generator is used to bias the readout electrode at a frequency slightly detuned from the resonance. These two signals generate a mix-down signal of mechanical origin at the readout electrode when the drive frequency matches exactly half the mechanical resonance frequency. This low-

frequency readout signal is amplified and fed into a lock-in amplifier (Signal Recovery model 5210) with a matching external reference generated from the two function generators.

For the MALDI work and ESI work with IgM, the modes were actuated using Agilent (model N5181A) and Rhode and Schwartz (SM03) function generators. For each mode the drive and bias signals were split. On one path, the bias and drive signals were mixed and the output used as the reference for the lock-in amplifier (Stanford Research Systems model SR830). On the other path, the drive signals for both modes were combined together with a DC source and the total signal ($V_1(\omega_{d1})$ + $V_2(\omega_{d2})$ + V_{DC}) was sent to the gate electrode that capacitively actuates the device. Meanwhile, the bias signals for each mode were split in a 180^0 splitter and the same-polarity signals of both modes were combined and sent to the device. At the device, the bias 1 electrode was charged to $V_1^+(\omega_{b1})$ + $V_2^+(\omega_{b2})$ and the bias 2 electrode to $V_1^-(\omega_{b1})$ + $V_2^-(\omega_{b2})$.   The control loop is implemented by reading the lock-in amplifier signal on a computer which performs a corrector calculation and then sends a control signal to the function generators. Details of the corrector calculation are given in Ref. [21]. The lock-in amplifiers and the function generators are connected to the computer by a GPIB interface. In this manner, the computer controls the instruments without being connected to the RF signals that are sent to the device. The GPIB interface, however, does limit the overall loop time to hundreds of milliseconds. New third-generation equipment has recently enabled demonstration of control loop times of less than ~100μs [22].

Figure S6| (a) Diagram of the MALDI experimental system. The NEMS resonator is located approximately 5mm away from the MALDI sample surface. **(b)** Diagram of the circuit used for the actuation and the readout of the NEMS device. In the diagram, PS = power splitter/combiner, 180 deg. PS = power splitter with 180 degree phase offset, LPF = low pass filter, in = input port to lock-in amplifier, ref= reference port of lock-in amplifier. The Bias and Drive oscillators are commercial frequency generators. The feedback loop is in blue. The signal from the Lock-In Amplifiers is read by a computer which, via a corrector calculation, sends a feedback signal to the bias and drive function generators.
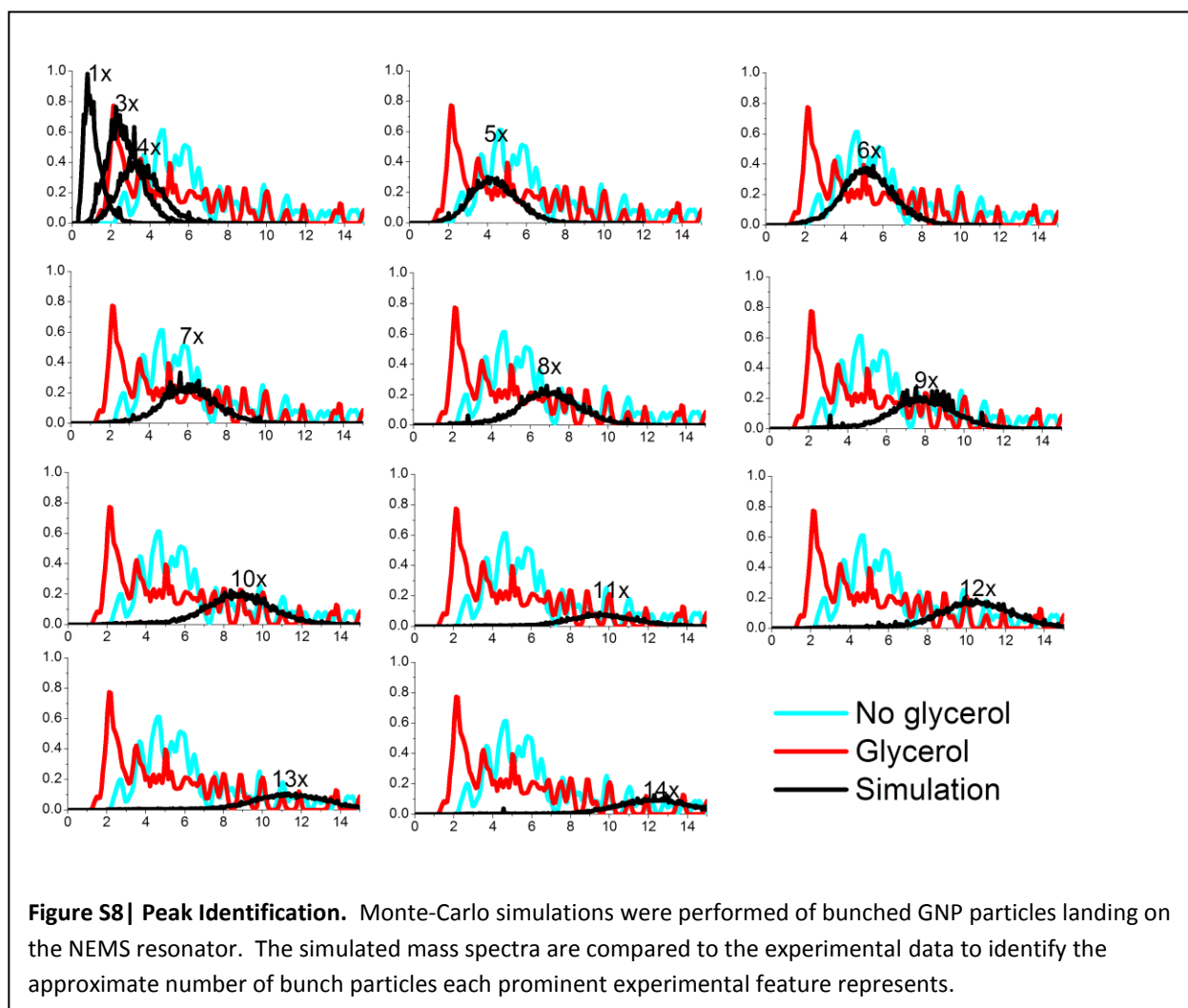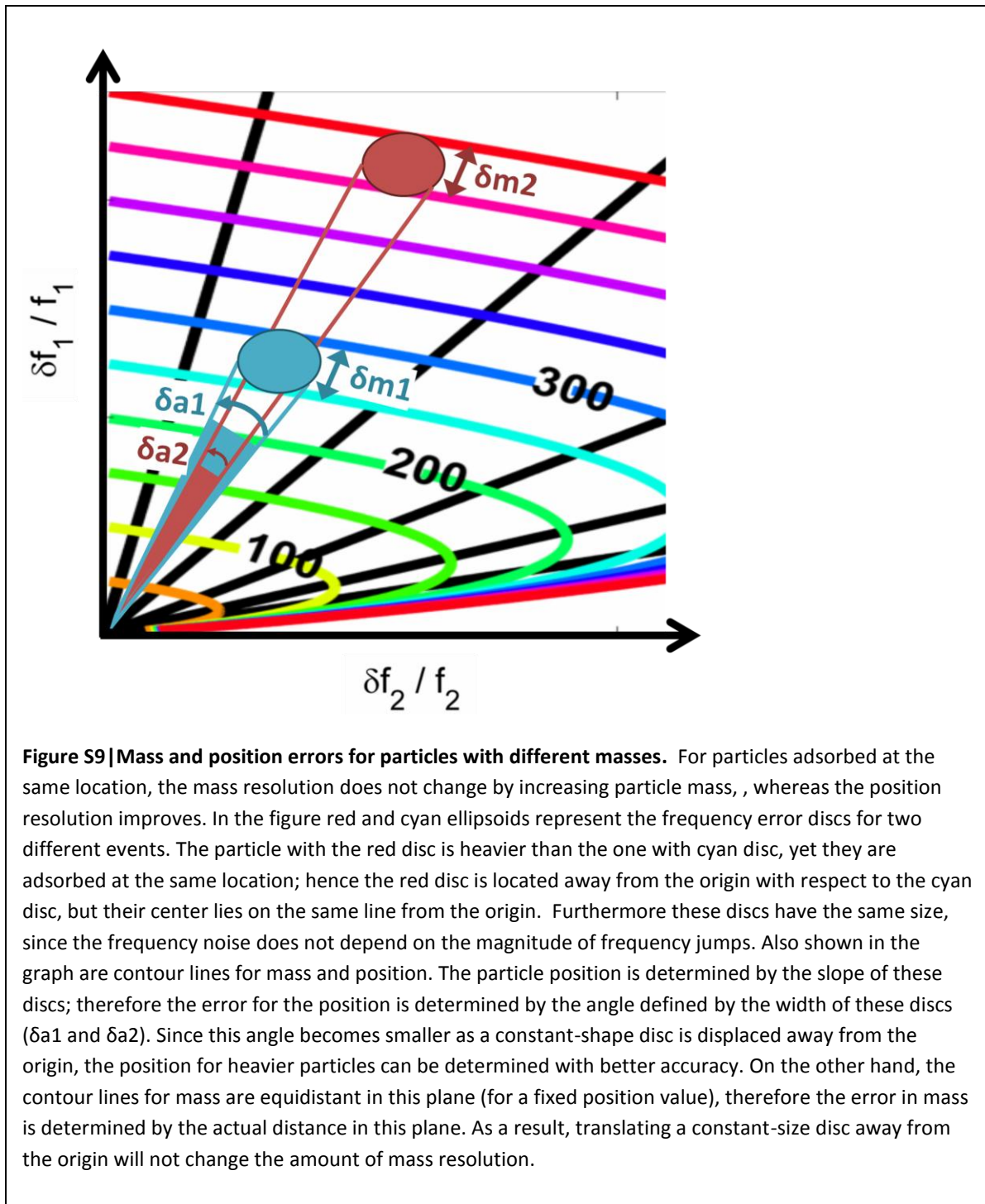
Fitting 10nm GNP data

Least-squares fitting was performed between the experimental data and mass histograms of theoretical nanoparticle distributions as the particle radius and standard deviation (assuming Gaussian size distribution) were varied. Figure S7 shows the error contours (log scale) with the radius in nm and the standard deviation as a percent of the radius. As seen from the contour graphs the minimum error is achieved for the ESI (MALDI) setups for radius = 4.90 (5.35) nm and standard deviation = 1.25 (1.4)nm.

Figure S7|Error fitting contours for 10nm GNP data. Sum of squared errors for the ESI (**a**), and MALDI (**b**) of the10nm GNP data as the fitting radius and standard deviation are varied. The error is plotted in log scale. The abrupt transitions in the error occur because for large fitting radius, the standard deviation has a large effect on the degree of overlap between the fitted and experimental mass curves compared to smaller values of the fitted radius. Nonetheless, the algorithm converges to a minimum error at values corresponding to vendor specifications for the samples.
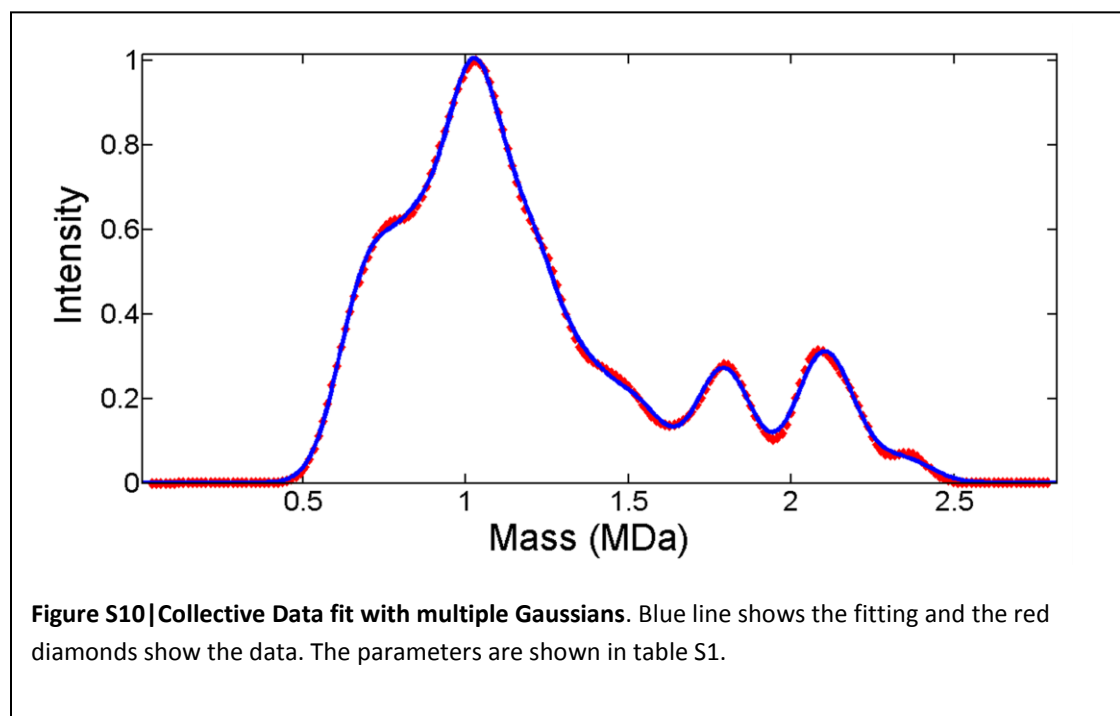
Peak identification in 5nm bunched GNP data

To identify the location of the mass peaks at the various bunching levels, Monte-Carlo simulations were performed of 5nm GNPs landing on the NEMS resonator to produce frequency jumps. These simulated jumps were then analyzed in the same way as the experimental data. In the simulations, the bunched particles had a total mass equal to the addition of some integer number of individual 5nm GNPs, each drawn from a size distribution based on the specifications of the vendor (Sigma Aldrich, mean diameter = 5.1nm, variance = 19% of average size). The simulated mass spectra were then compared with the experimental data and the center of the simulated peaks was found to coincide with the position of the various peaks in the data. Figure S8 shows panels of the same experimental data overlaid with the simulated spectra to show the matching between the peak locations.

Figure S8| Peak Identification. Monte-Carlo simulations were performed of bunched GNP particles landing on the NEMS resonator. The simulated mass spectra are compared to the experimental data to identify the approximate number of bunch particles each prominent experimental feature represents.

Figure S9|Mass and position errors for particles with different masses. For particles adsorbed at the same location, the mass resolution does not change by increasing particle mass, , whereas the position resolution improves. In the figure red and cyan ellipsoids represent the frequency error discs for two different events. The particle with the red disc is heavier than the one with cyan disc, yet they are adsorbed at the same location; hence the red disc is located away from the origin with respect to the cyan disc, but their center lies on the same line from the origin. Furthermore these discs have the same size, since the frequency noise does not depend on the magnitude of frequency jumps. Also shown in the graph are contour lines for mass and position. The particle position is determined by the slope of these discs; therefore the error for the position is determined by the angle defined by the width of these discs ($\delta a1$ and $\delta a2$). Since this angle becomes smaller as a constant-shape disc is displaced away from the origin, the position for heavier particles can be determined with better accuracy. On the other hand, the contour lines for mass are equidistant in this plane (for a fixed position value), therefore the error in mass is determined by the actual distance in this plane. As a result, translating a constant-size disc away from the origin will not change the amount of mass resolution.

Fitting for the IgM Ensemble

Single molecule events during the IgM run were assigned to the specific oligomers of the protein (also called IgM isoforms) by using the peak of their mass probability distribution. In a small number of the cases, some of these events could be incorrectly assigned if the noise during the measurement exceeds the two-sigma level (100kDa) which is the threshold for separating different oligomers. Here, we use an alternative method to make these assignments by using the overall spectrum of the 73 events and fitting it with multiple Gaussians, each representing the contribution of one specific oligomer (we did not consider the single event at 3.6MDa in this analysis). The weight and the mean of each of the Gaussian were varied in the fitting until the sum of squared errors was minimized. The dispersion of each of the Gaussians was kept the same, as expected from the measurement. Below in Figure S11 we compare the result of the fitting with the data. The parameters extracted both from this analysis and the single event approach are shown and compared in table S1. Five particles out of 73 were assigned to different oligomers between these two approaches. As the signal-to-noise ratio increases in the future experiments, the two approaches should converge to the same values.

Figure S10|Collective Data fit with multiple Gaussians. Blue line shows the fitting and the red diamonds show the data. The parameters are shown in table S1.

Species	Percentage (Ensemble Analysis)	Percentage (Single Molecule)	Difference in Percentages	Number of Particles (Ensemble Analysis)	Number of Particles (Single Molecule)	Extracted mass value Collective (MDa)
M3	13.5	9.5	4.0	10	7	0.69
M4	14.0	16.5	-2.5	10	12	0.86
M5	26.5	27.0	-0.5	19	20	1.03
M6	14.6	14.3	0.3	11	10	1.20
M7	6.6	7.6	-1.0	5	5	1.37
M8	5.0	3.5	1.5	4	3	1.53
M9	8.2	7.6	0.6	6	6	1.79
M10	8.5	8.4	0.1	6	6	2.09
M11	1.6	3.8	-2.2	1	3	2.16
M12	1.6	1.9	-0.3	1	1	2.35

Table 1: Decomposition parameters for the IgM using the ensemble analysis and single-molecular approach. The collective histogram is fitted to multiple Gaussians. The best fit parameters are reported here as the percentages of the isoform in the ensemble. These values are also converted to expected number of particles and compared with the single-molecule scale analysis. The mean values for the Gaussian distributions are used as the expected masss values (last column) and these agree with the expected isoform values.
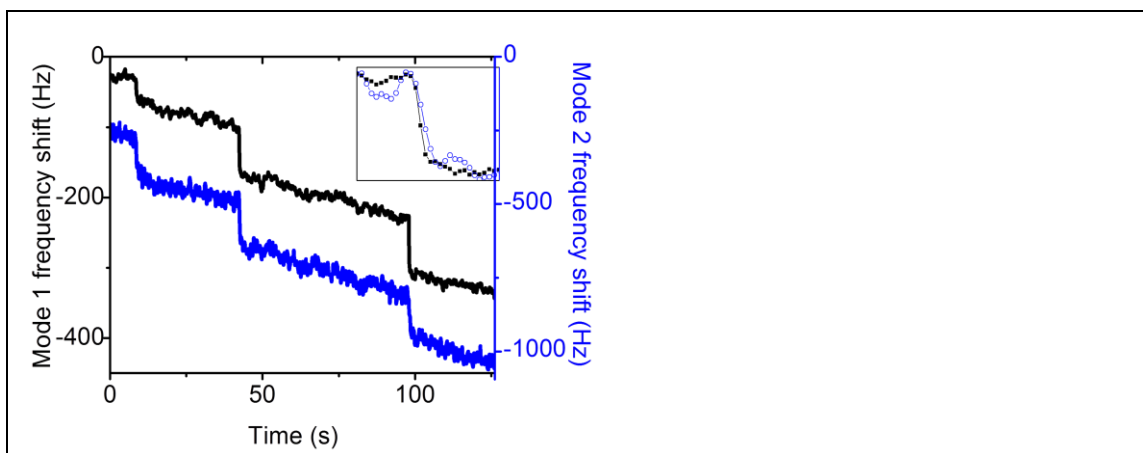
Figure S11| Frequency jumps due to IgM adsorption. The black (blue) curve shows the first (second) mode frequency in real time. As IgM molecules land on the device, the frequency of the both modes jumps down within the PLL timescale. A frequency offset of 27.4MHz (72.6 MHz) is subtracted from the first(second) mode. **Inset:** one of the frequency jumps is shown in detail. Here the frequency jump is clearly resolved with the data acquisition system sampling at 100ms (black squares and blue circles).
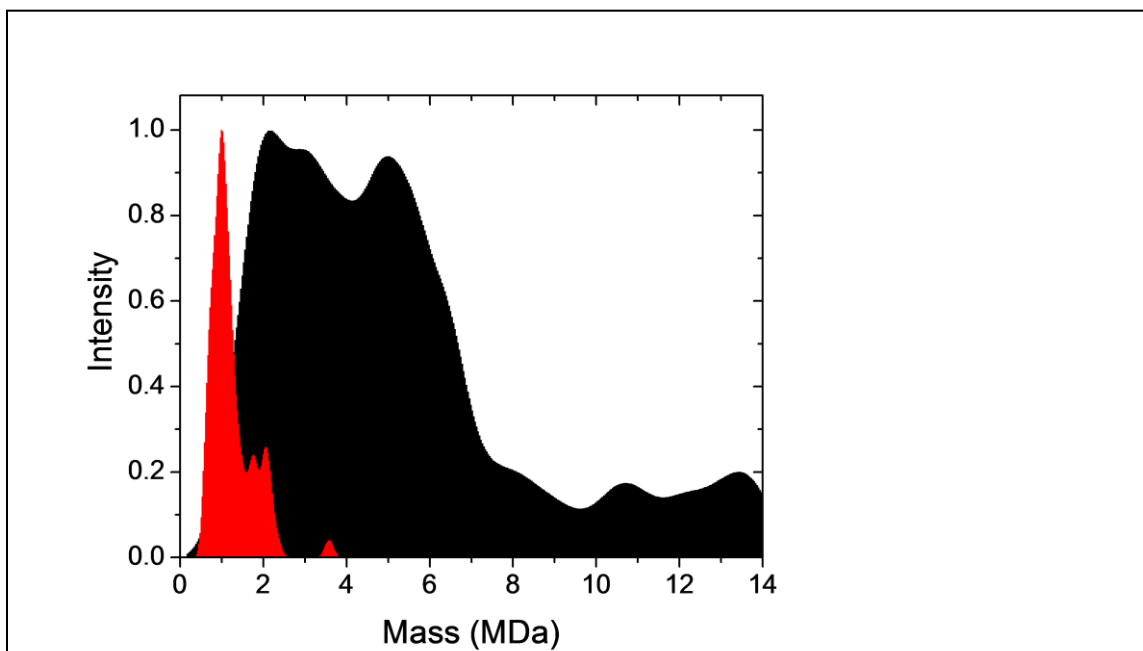

Figure S12|Comparison of IgM and 10-nm GNP Mass Spectrum. The composite IgM spectrum (ESI setup) is shown in red as a narrow distribution at the low mass region. 10-nm GNP spectrum (MALDI setup) is shown in black. It is obvious that the IgM spectra is much narrower than the GNP spectra.

References

1   Naik, A. K., Hanay, M. S., Hiebert, W. K., Feng, X. L. & Roukes, M. L. Towards single-molecule nanomechanical mass spectrometry. *Nat Nano* **4**, 445-450 (2009).

2   Yang, Y. T., Callegari, C., Feng, X. L. & Roukes, M. L. Surface Adsorbate Fluctuations and Noise in Nanoelectromechanical Systems. *Nano Letters* **11**, 1753-1759, doi:10.1021/nl2003158 (2011).

3   Atalaya, J., Isacsson, A. & Dykman, M. I. Diffusion-Induced Bistability of Driven Nanomechanical Resonators. *Physical Review Letters* **106**, 227202 (2011).

4   Atalaya, J., Isacsson, A. & Dykman, M. I. Diffusion-induced dephasing in nanomechanical resonators. *Physical Review B* **83**, 045419 (2011).

5   Maizelis, Z. A., Roukes, M. L. & Dykman, M. I. Detecting and characterizing frequency fluctuations of vibrational modes. *Physical Review B* **84**, 144301 (2011).

6   Hanay, M. S. *Towards Single-Molecule Nanomechanical Mass Spectrometry* Doctor of Philosophy thesis, California Insitute of Technology, (2011).

7   Allan, D. W. Statistics of atomic frequency standards. *Proceedings of the IEEE* **54**, 221-230 (1966).

8   Roe, B. P. *Probability and statistics in experimental physics*. (Springer-Verlag, 1992).

9   Casella, G. & Berger, R. L. *Statistical Inference*. 2 edn, (Duxbury Press, 2001).

10 Dole, M. *et al. Molecular Beams of Macroions*. Vol. 49 (AIP, 1968).

11 Fenn, J., Mann, M., Meng, C., Wong, S. & Whitehouse, C. Electrospray ionization for mass spectrometry of large biomolecules. *Science* **246**, 64-71, doi:10.1126/science.2675315 (1989).

12 Bargatin, I., Kozinsky, I. & Roukes, M. L. Efficient electrothermal actuation of multiple modes of high-frequency nanoelectromechanical resonators. *Applied Physics Letters* **90**, 093116-093113, doi:10.1063/1.2709620 (2007).

13 Li, M., Tang, H. X. & Roukes, M. L. Ultra-sensitive NEMS-based cantilevers for sensing, scanned probe and very high-frequency applications. *Nat Nano* **2**, 114-120 (2007).

14 Karas, M., Bachmann, D. & Hillenkamp, F. Influence of the wavelength in high-irradiance ultraviolet laser desorption mass spectrometry of organic molecules. *Analytical Chemistry* **57**, 2935-2939, doi:10.1021/ac00291a042 (1985).

15 Tanaka, K. The Origin of Macromolecule Ionization by Laser Irradiation (Nobel Lecture). *Angewandte Chemie International Edition* **42**, 3860-3870, doi:10.1002/anie.200300585 (2003).

16 Mile, E. & et al. In-plane nanoelectromechanical resonators based on silicon nanowire piezoresistive detection. *Nanotechnology* **21**, 165504 (2010).

17 Bargatin, I. *et al.* Large-Scale Integration of Nanoelectromechanical Systems for Gas Sensing Applications. *Nano Letters*, doi:10.1021/nl2037479 (2012).

18 *Caltech/CEA-LETI Alliance for Nanosystems VLSI, 200mm (second-generation) Standard NEMS Process: "CAL2".* , <http://www.nanovlsi.com> (

19 Cole, R. B. *Electrospray and MALDI Mass Spectrometry*. (Wiley, 2010).

20 Bargatin, I., Myers, E. B., Arlett, J., Gudlewski, B. & Roukes, M. L. Sensitive detection of nanomechanical motion using piezoresistive signal downmixing. *Applied Physics Letters* **86**, 133109 (2005).

21 Kharrat, C., Colinet, E. & Voda, A. in *Sensors, 2008 IEEE.* 1135-1138.

22 Colinet, E., Sage, E., Myers, E. B. & Roukes, M. L. *(Unpublished Work)*.